

Probing p -wave superconductivity in UTe_2 via point-contact junctions

Hyeok Yoon,^{1,2} Yun Suk Eo,^{1,2} Jihun Park,^{1,3} Jarryd A. Horn,^{1,2} Ryan G. Dorman,^{1,2} Shanta R. Saha,^{1,2} Ian M. Hayes,^{1,2} Ichiro Takeuchi,^{1,3} Philip M. R. Brydon,⁴ and Johnpierre Paglione^{1,2,*}

¹Maryland Quantum Materials Center, University of Maryland, College Park, MD 20742, USA

²Department of Physics, University of Maryland, College Park, MD 20742, USA

³Department of Materials Science and Engineering, University of Maryland, College Park, MD 20742, USA

⁴Department of Physics and MacDiarmid Institute for Advanced Materials and Nanotechnology, University of Otago, P.O. Box 56, Dunedin 9054, New Zealand

Here we perform a spectroscopic study of the ambient pressure superconducting phase of UTe_2 , measuring conductance through point-contact junctions formed by metallic contacts on different crystalline facets down to 250 mK and up to 18 T. Fitting a range of qualitatively varying spectra with a Blonder-Tinkham-Klapwijk (BTK) model for p -wave pairing, we can extract gap amplitude and interface barrier strength for each junction, and best model the data with a purely p_y -wave gap function with amplitude in the range 0.2 - 0.35 meV. Our work provides a spectroscopic confirmation of the spin-triplet superconducting gap in UTe_2 , and confirms that a topologically non-trivial superconducting order parameter is likely.

I. INTRODUCTION

The recent discovery of spin-triplet superconductivity in UTe_2 [1] has raised the possibility of realizing the technological dream of odd-parity pairing with non-trivial topology in a natural solid state material. The strongest signatures of triplet pairing in UTe_2 include upper critical fields greatly exceeding Pauli limits for each crystal orientation [1], re-entrant superconductivity in ultra-high magnetic fields [2], and near absence of changes in the NMR Knight shift below the superconducting transition temperature [1, 3, 4]. Together with the observation of chiral in-gap states revealed by scanning tunneling microscopy (STM) studies [5] and a normal surface fluid identified in microwave impedance measurements [6], these ingredients provide strong evidence for the non-trivial topological nature of superconductivity in UTe_2 .

The intrinsic symmetry of the superconducting order parameter, which requires identification in order to understand both the pairing mechanism as well as the nature of topological excitations, belongs to the irreducible representation of the point group of the material's crystal structure (D_{2h}). Assuming spin-triplet pairing, the orbital component of the order parameter should be odd, constraining the possible candidates to A_u (full-gap), B_{iu} ($i=1,2,3$; point-nodes), and their combinations [7, 8]. Experimental studies on the first generation of UTe_2 crystals proposed a multi-component order parameter, i.e. $B_{3u} + iB_{2u}$ or $A_u + iB_{1u}$, based on the observation of nodal excitations in thermal transport [9], broken time-reversal symmetry (TRS) in polar Kerr effect experiments and two distinct superconducting transitions in specific heat [10]. However, later generation materials with higher T_c values appear to have only a single thermodynamic transition, a small but finite Knight shift [3, 4], and an apparent lack of TRS breaking [11], raising the possibility that a two-component order parameter is not an intrinsic property of UTe_2 [12–14]. Ultimately, the lack of a jump in elastic shear moduli in both generations of materials [15] points conclusively to a single-

component order parameter, but is still inconsistent with the observation a quadratic temperature dependence of magnetic penetration depth for all crystallographic directions [9, 16].

Spectroscopic studies have historically been very decisive in determining superconducting order parameter symmetry. In UTe_2 , STM studies by four independent groups have successfully probed the cleaved surface and the superconducting gap at the Fermi level [5, 17–21], but have only studied the easy-cleavage plane (011) [5, 17–19] and the (001) surface [21]. More important, studies of the gap structure by STM have been hindered by the abundance of in-gap states that fill in a large fraction of the differential conductance, which remains a mystery but is likely affected by the presence of surface states such as charge- [17, 18] and pair-density wave orders [19], as well as the anomalous non-superconducting fluid at the surface [6].

An alternative approach to studying the directional nature of the superconducting order parameter is to fabricate normal-metal/(insulator)/superconductor (N-(I)-S) junctions in which facets are defined by oriented polishing of bulk single crystals, and performing spectroscopic tunneling experiments. However, to date the realization of a functional device has been a challenge due to the lack of understanding of surface oxidation and interface quality. In this study, we present the successful measurement of energy spectra in Au/Ti/ UTe_2 planar junctions formed on two different facet orientations by utilizing the surface oxidation layer of UTe_2 . The observed conductance spectra are well described by a p -wave BTK model for tunneling into triplet superconductors and suggest a p_y -wave symmetry as the most plausible order parameter for the ambient pressure superconductivity of UTe_2 .

II. METHODS

Single crystals of UTe_2 were grown by the chemical vapor transport method [1, 22], yielding samples with a transition temperature $T_c = 1.6$ K. Orientation of crystal facets was determined using the anisotropy in magnetic susceptibility. Facets on two samples (S1 with (001) facet, and S2 with

* correspondence to: paglione@umd.edu

facet normal vector $\hat{n} = [0.4, 0.6, 0.7]$; see SI, section I.) were polished using aluminum oxide lapping films, and metal contacts were fabricated using Au thin films deposited by evaporation followed by 3-5 nm of Ti adhesive metal. S1 and S2 were patterned by conventional lithography, with details of the fabrication process and dimensional parameters described in SI, section II. During fabrication, samples are heated at 100 °C for 1 minute for baking photoresist and additionally heated at 100 - 120 °C for 2-3 minutes to adhere glue to a cover glass. In-Sn solder was used to make ohmic contacts to samples. The final device structure is shown in Fig. 1(a). For the electrical measurements, transport and differential conductance measurements were performed using a ^3He commercial probe with base temperature of 300 mK.

III. RESULTS

Our point-contact junctions incorporate the native oxide of UTe_2 that forms upon exposure to air. The baking process of photoresist during the fabrication further enhances the surface oxidation, making its thickness more than tens of nanometers [23]. Despite the thick oxidation layer, our junction resistances maintain low ($R_c < 10 \Omega$) values at low temperatures. However, considering the nature of the oxidation layer, it is likely that there exists metallic shorts through the layer that form leaking paths in large-size N-I-S planar junctions that decrease the effective size of junctions, thereby suppressing inelastic electron scattering across the junctions (Fig. 1(a)). In this ballistic regime, the spectra can reflect the energy density of states of the sample layer as shown in many other cases

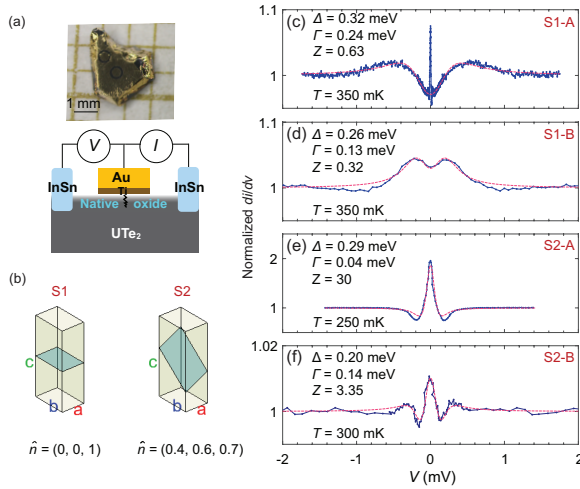


FIG. 1: The differential conductance spectra measured at the UTe_2 junctions at the base temperature of ^3He system. (a) The schematic of point-contact devices. (b) The graphical representation of facets of S1 and S2. (c)-(f) the normalized differential conductance (blue) and their fits using p -wave BTK formula (pink). The parameters for fit Δ , Γ , Z , and T are noted. Here, T is set the same as the measurement temperature. Z is a fitting parameter except for S2-A.

[24–29]. Despite the inability to form a proper tunnel barrier, we can therefore utilize this configuration to perform point-contact spectroscopy.

Figure 1 and 2 show the differential conductance spectra across the junctions (S1-A, S1-B, S2-A, S2-B) at the base temperature and their temperature evolution. Here, S1 and S2 label the crystals, and A and B label the junctions. For example, S1-A is the junction A fabricated on the crystal S1. S1-A and S1-B are fabricated on the same facet (001) of the crystal S1, and S2-A and S2-B are created on the opposing faces of crystal S2, which run parallel to each other. Figure 1(b) presents a schematic of the facets of the junctions on samples S1 and S2, demonstrating the different orientation of the conductance measurements for each sample. In Fig. 1(c)-(f), spectra are normalized to the normal-state spectra above T_c . As shown in Fig. 2, features in the differential conductance spectra are developed below the superconducting transition temperature and the upper critical field for all junctions, and the details of each spectra are described below.

All junctions presented in this study exhibit spectral features consistent with a gap opening below $T_c = 1.6$ K in these crystals of UTe_2 . Sample S1-A exhibits a dip feature at an energy close to the expected superconducting gap energy $\Delta = 0.25$ meV, estimated from the weak-coupling BCS the-

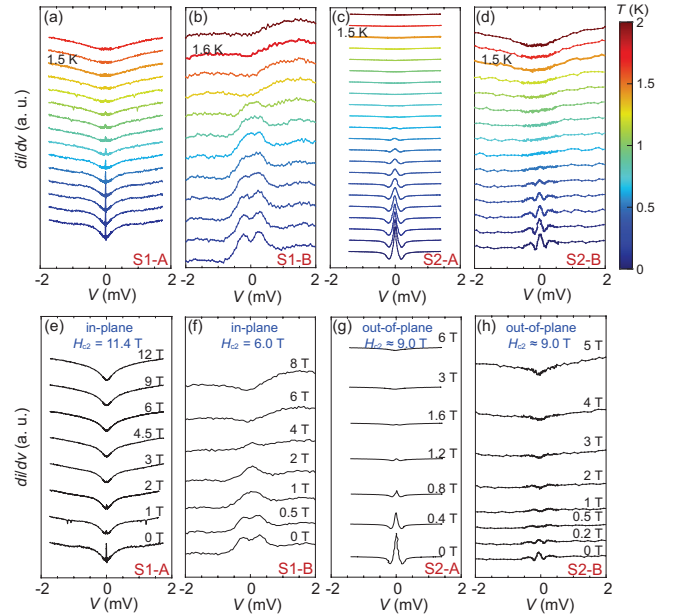


FIG. 2: Temperature and magnetic field dependence of the differential conductance of UTe_2 junctions (a)-(d) Temperature dependence of di/dv at $B = 0$ T. For each panel, the $T = 1.5$ K or 1.6 K data are labeled to denote the resistive transition temperature. (e)-(h) Magnetic field dependence of di/dv at base temperatures. For S1-A and S1-B, the magnetic field is applied in-plane, and the upper critical field is obtained from the measurement in resistive transition. For S2-A and S2-B, the magnetic field is applied out-of-plane, and the upper critical field is roughly estimated based on the orientation of facets.

ory (*i.e.*, $2\Delta/k_B T_c = 3.56$), with shoulders reminiscent of coherence peaks in the superconducting density of states. However, this sample also exhibits a prominent peak at zero-bias, as shown in Fig. 1(c). The coherence peaks vanish in the vicinity of T_c , and the parabolic background remains in the normal state spectra. On the other hand, when the magnetic field is applied in-plane (15° off from the b -axis), the coherence peak disappears. We note that determining when exactly the coherence peaks disappear is not clear since the background dip structure is deeper and remains even beyond $\mu_0 H_{c2} = 11.4$ T, in contrast to the normal-state spectra above T_c . While the zero-bias peak (ZBP) is a very interesting feature that could possibly be associated with zero-energy Andreev states which occur in a topological superconductor, we first note that its energy width is narrower than the minimum broadening possible due to the thermal smearing of the spectra; the peak width is ~ 10 μeV while $k_B T = 25$ μeV at $T = 300$ mK. Out of many possible reasons for the ZBP in the differential conductance [30], to our knowledge the only source immune to thermal broadening is from a Josephson supercurrent across the junction. This is an interesting aspect of sample S1-A that was not reproduced in other junctions, and may be an indication of a tunneling phenomenon. However, it is important to note that our Au/Ti counter-electrode is not nominally superconducting, raising the question of what component plays the role of a superconducting electrode in such a SNS or SIS Josephson configuration [31].

Sample S1-B, which is a separate junction on the same crystal facet as S1-A, exhibits a different shape consisting of a small dip imposed on a broad conductance enhancement (Fig. 1(d)). In addition, we also see a weak dip in conductance at energies higher than the low-energy enhancement. This combined peak-dip structure is often observed in the thermal regime of contacts and can be explained by the influence of the critical current, causing the system to transition into a high-resistance state before the local superconductivity is suppressed [32–35]. In this case, the small dip represents the energy spectra imposed on the broad peak due to the superconductivity. The energy scale of this dip feature matches the superconducting gap size Δ (~ 0.2 meV) of UTe_2 , which is consistent with this scenario. Note that the peak-dip feature has also been observed in other materials such as $\text{Pt-Sr}_2\text{RuO}_4$ point-contact junctions, but was explained in a different manner by incorporating a phenomenological transmission cone instead of attributing the structure to critical current effects [36]. This model suggests that it could be also feasible to fit our S1-B junction without taking the critical current into account.

Sample S2-A exhibits a peak-dip structure as well, but with a very sharp ZBP and dips on either side at higher energies. The strong ZBP has amplitude nearly twice as large as the background as shown in Fig. 1(e), and is often seen in point-contact junctions and explained via various origins. First, the ZBP may result from the prevalent Andreev reflection. However, the distinctive dip outside this ZBP can not be explained solely with Andreev reflection, so we rule out this case. Second, the peak-and-dip structure can be interpreted as the effect of critical current, as discussed in the section for S1-

B. Nonetheless, we exclude this scenario because the background of the spectra is neither T nor B dependent, clearly indicating that the transport-like conduction in the thermal regime is negligible. In addition, if the dip and ZBP structure arises from the critical current, the dip should be spike-like and its position should shift to the center as T or B increases, as reflecting the features of the critical current. In contrast, the width of the ZBP in our spectra does not change significantly with increasing T or B (Fig. 2(c)-(g)). Also, in our case, the peak intensity is sharply suppressed as T or B increases, contrasting with the binary character of the resistive transition. Hence, we attribute the ZBP to the existence of surface Andreev-bound states often observed in the tunneling limit. This ZBP originates from the interference of the transmitted electron-like quasi-particle and hole-like quasi-particle experiencing the phase difference of the pair potential [37, 38]. This constructive interference can be induced when the electrons are injected along the nodal direction of d -wave superconductors [39] or in the p -wave topological superconductors [40, 41].

Finally, for sample S2-B, the spectrum has similar features to both S1-B and S2-A, but with much smaller ZBP intensity as compared to S2-A as shown in Fig. 1(f). The varying features in the four spectra present differing behavior that are actually useful for identifying distinct responses due to gap structure, and can be reasonably well modeled by variations of junction parameters using a p -wave gap scenario as explained below.

To model these conductance spectra, we have utilized a generalization of the BTK theory [42] for tunneling into triplet superconductors [43], calculating the conductance according to the formula

$$\frac{dI}{dV} = \sigma_N \int_{-\infty}^{\infty} \sigma_{\text{BTK}}(E + i\Gamma) \left[-\frac{\partial f(E + eV)}{\partial E} \right] dE \quad (1)$$

where σ_N is the normal-state tunneling conductance, $\sigma_{\text{BTK}}(E)$ is the normalized BTK conductance, $f(E)$ is the Fermi function, and Γ is a phenomenological broadening parameter. Details of the calculation are presented in the supplemental material (see SI, section IV). The orthorhombic crystal symmetry of UTe_2 places few constraints on the structure of the triplet pairing states in each irrep: even upon restricting to p -wave gap symmetry, a general pairing state has two (B_{iu} , $i = 1, 2, 3$) or three (A_u) independent p -wave gap components. To keep our task manageable we assume that the pairing state preserves TRS. Our fitting parameters hence consist of the relative strength of the different p -wave components, the overall gap amplitude Δ , the interface barrier strength Z , and Γ . We find that the data is most consistent with a purely p_y -wave gap function $\Delta(\mathbf{k}) = \Delta_0 k_y / k_F$ with zero-temperature gap amplitude in the range 0.2 to 0.35 meV. This is consistent with values of $\Delta = \pm 0.25$ meV obtained by spectroscopic STM experiments on the [011] crystalline surface [5]. Although we cannot exclude the presence of other symmetry-allowed p -wave gap components, our analysis suggests that they are small.

The ZBP offers an important clue to gap structure of an un-

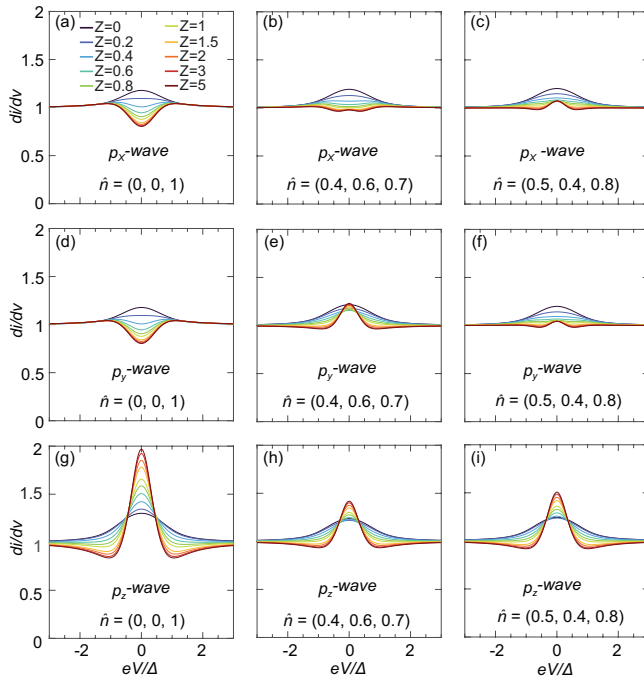


FIG. 3: BTK simulation of normalized differential conductance at different facets using p -wave model.

(a)-(c), (d)-(f), (g)-(i) show the BTK simulation with p_x , p_y , p_z , respectively. (a),(d),(g) are BTK simulation at the facet $\hat{n} = [0, 0, 1]$. (b), (e), (h) are BTK simulation at the facet $\hat{n} = [0, 4, 0.6, 0.7]$. (c), (f), (i) are BTK simulation at the facet $\hat{n} = [0, 5, 0.4, 0.8]$. Different colors represent different Z parameters. Z sweeps from 0 to 5 as colors changes from blue to red. We choose $k_B T = 0.1\Delta$ and $\Gamma = 0.4\Delta$.

conventional superconductor: a pronounced ZBP typically indicates zero-energy surface Andreev bound states, which occur when the superconducting gap changes sign upon reversing the momentum component normal to the surface; on the other hand, the absence of the ZBP is consistent with a gap which does not change sign upon this reversal. For a p -wave superconductor the differential conductance is anisotropic; in particular, the presence or absence of a ZBP at a given surface is characteristic of different p -wave gaps. To visualize this concept, Fig. 3 demonstrates the normalized differential conductance spectra for the facets of our samples, simulated from the BTK theory using a p -wave model. As shown in Fig. 3 (a), (d), and (g), the gap-like feature around zero-bias in the (001) S1-A and S1-B conductance data is thus not consistent with a dominant p_z -wave gap component, and indeed can be reasonably fit by a purely p_x - or p_y -wave gap.

On the other hand, as shown in Fig. 3 (b), (e), and (h), a purely p_z - or p_y -wave state gives the best fit to the sharp ZBP in the S2-A data, consistent with the surface normal lying 23° away from the y - z plane. We note that the prominence and height of the peak is enhanced by reducing the broadening Γ , which in Fig. 3 is several times larger than in our fit to the S2-A data. Since the S1 data excludes a dominant p_z -wave component, this implies that the gap is predominantly

p_y -wave in character.

The S2-B case is least consistent with a purely p_y -wave gap, and a better fit is obtained for a p_x -wave state. Although this is hard to reconcile with the S2-A data for nominally the same surface normal, assuming a slight misalignment of the surface normal compared to the S2-A surface yields an excellent fit to a purely p_y -wave gap. Specifically, best agreement is obtained for an approximately 10° misalignment ($\hat{n} = [0, 5, 0.4, 0.8]$), which is shown in Fig. 3 (c), (f) and (i). This degree of misalignment is experimentally possible since S2-B is fabricated on the other side of S2-A, possibly making the two facets not exactly parallel.

The variation of the fitted gap amplitude with temperature is shown in Fig. 4. The S1-A data follows rather closely the weak-coupling temperature dependence of a p -wave pairing state with $T_c = 1.6$ K; the S1-B data shows a similar variation albeit with somewhat lower critical temperature. In contrast, the S2-A and S2-B data show an approximately linear decline in the gap as a function of temperature, extrapolating to zero for $T_c \leq 1$ K, which suggests a lower T_c at the surface.

Our theoretical analysis has utilized a number of standard simplifying assumptions. In particular, we treat the Fermi surface in both the lead and superconductor as spherical with the same Fermi wavevector and effective mass. Although this is inconsistent with the quasi-2D Fermi surface and significant orthorhombic anisotropy in normal-state resistivity in

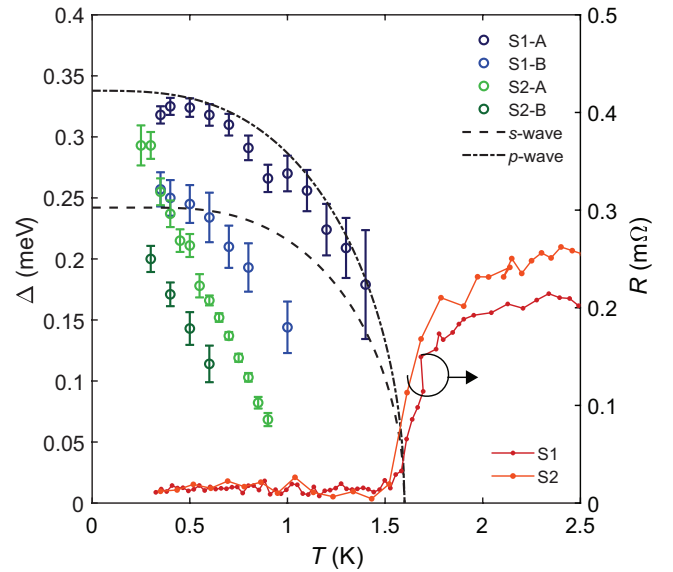


FIG. 4: The superconducting gap size over temperature Circles represent the gap sizes extracted from the p -wave BTK fits. The errorbar is defined by the 95% confidence interval for the fit. The dashed and dotted curves are the simulated temperature dependence of gap-size in s -wave and p -wave model, respectively, with $T_c = 1.6$ K. The red and orange curves, measured in S1 and S2, respectively, demonstrate the superconducting transition measured by four-probe resistance using the ohmic contacts as a current leads and point-contacts for voltage leads.

UTe₂, accurately accounting for the band structure typically does not introduce significant quantitative changes in the BTK theory predictions [44]. However, the unexpected linear T -dependence of the gaps measured at the S2 surfaces may indicate a breakdown of our BTK theory. In particular, we have neglected the variation of the gap near the surface of the material, which could be significant at the S2 surfaces of our proposed p_y -wave state. Accounting for this might alter the quantitative values of our fit parameters but is not expected to qualitatively alter our conclusions; in particular, the relation between the ZBP and the gap symmetry can be formulated in terms of topological invariants [45], making this feature somewhat immune to details of the surface.

In summary, we have presented point-contact spectroscopy spectra of the superconducting state of UTe₂ using four distinct junctions fabricated by depositing Ti/Au metal contacts on the native oxide surface of UTe₂ single crystals with two different facet orientations. By fitting conductance spectra measured with currents directed along both ($\hat{n} = [0, 0, 1]$) and ($\hat{n} = [0, 4, 0.6, 0.7]$), we are able to model the data with a simple p -wave BTK model, extracting gap amplitude and constraining the gap structure. All junctions exhibit gap-like features that close at the superconducting transition temperature and upper critical field of UTe₂, with energies in the range 0.2 to 0.35 meV consistent with energy scales observed in scanning tunneling spectroscopy and derived from thermodynamic quantities. Upon careful examination of a p -wave BTK model, we conclude that a gap with a dominant p_y -wave component is the most consistent with our data. Our study demonstrates the potential of performing electronic spectroscopy in UTe₂ in a stable device with choice of crystalline facet direction and external environment, opening the door to further studies of the multiple superconducting phases of UTe₂, including the re-entrant and field-polarized states.

ACKNOWLEDGMENTS

We have benefited from discussions with Daniel F. Agterberg. Research at the University of Maryland was supported by the U.S. Department of Energy Award No. DE-SC-0019154 (sample characterization), the Air Force Office of Scientific Research under Grant No. FA9950-22-1-0023 (spectroscopic experiments), the Gordon and Betty Moore Foundation's EPiQS Initiative through Grant No. GBMF9071 (materials synthesis), and the Maryland Quantum Materials Center. S.R.S. acknowledges support from the National Institute of Standards and Technology Cooperative Agreement 70NANB17H301. P.M.R.B. was supported by the Marsden Fund Council from Government funding, managed by Royal Society Te Apārangi, Contract No. UOO1836.

-
- [1] S. Ran, *et al.*, *Science* **365**, 684 (2019).
- [2] S. Ran, *et al.*, *Nat. Phys.* **15**, 1250 (2019).
- [3] G. Nakamine, *et al.*, *J. Phys. Soc. Jpn.* **88**, 113703 (2019).
- [4] H. Matsumura, *et al.*, *J. Phys. Soc. Jpn.* **92**, 063701 (2023).
- [5] L. Jiao, *et al.*, *Nature* **579**, 523 (2020).
- [6] S. Bae, *et al.*, *Nat. Commun.* **12**, 2644 (2021).
- [7] T. Shishidou, H. G. Suh, P. M. R. Brydon, M. Weinert, D. F. Agterberg, *Phys. Rev. B* **103**, 104504 (2021).
- [8] J. Ishizuka, S. Sumita, A. Daido, Y. Yanase, *Phys. Rev. Lett.* **123**, 217001 (2019).
- [9] T. Metz, *et al.*, *Phys. Rev. B* **100**, 220504 (2019).
- [10] I. M. Hayes, *et al.*, *Science* **373**, 797 (2021).
- [11] M. O. Ajeesh, *et al.*, *Phys. Rev. X* **13**, 041019 (2023).
- [12] S. M. Thomas, *et al.*, *Phys. Rev. B* **104**, 224501 (2021).
- [13] P. F. S. Rosa, *et al.*, *Commun. Mater.* **3**, 33 (2022).
- [14] H. Sakai, *et al.*, *Phys. Rev. Mater.* **6**, 073401 (2022).
- [15] F. Theuss, *et al.*, arxiv:2307.10938 (2023).
- [16] K. Ishihara, *et al.*, *Nat. Commun.* **14**, 2966 (2023).
- [17] A. Aishwarya, *et al.*, arxiv:2207.09491 (2023).
- [18] A. Aishwarya, *et al.*, *Nature* **618**, 928 (2023).
- [19] Q. Gu, *et al.*, *Nature* **618**, 921 (2023).
- [20] A. LaFleur, *et al.*, arxiv:2308.03721 (2023).
- [21] Y. Hu, presented at aps march meeting 2022, a61.00005 (2022).
- [22] S. Ran, *et al.*, *J. Vis. Exp.* (2021).
- [23] H. Yoon, presented at aps march meeting 2024, z02.00007 (2024).
- [24] I. Yanson, *J. Exp. Theor. Phys.* **39**, 506 (1974).
- [25] Y. G. Naidyuk, I. K. Yanson, Point-contact spectroscopy (2003).
- [26] I. Hwang, *et al.*, *Nanoscale* **7**, 8531 (2015).
- [27] H. Srikanth, A. K. Raychaudhuri, *Phys. Rev. B* **45**, 383 (1992).
- [28] M. Dvoranová, *et al.*, *AIP Adv.* **8**, 125217 (2018).
- [29] T. Hagiwara, O. Mizuno, S. Tanaka, *J. Phys. Soc. Jpn.* **34**, 973 (1973).
- [30] L. Kuerten, *et al.*, *Phys. Rev. B* **96**, 014513 (2017).
- [31] For our junctions, whereas the ZBP ceases to exist at around T_c , it disappears earlier than $\mu_0 H_{c2}$ at around 3.5 T in response to the in-plane magnetic field. The maximum value of the ZBP has an oscillation with respect to the in-plane magnetic field, which resembles the Fraunhofer pattern shown in the Josephson junction (SI, section III.). This observation supports the Josephson supercurrent hypothesis as the origin of the ZBP. The estimated junction area is $0.008 \mu\text{m}^2$ when the first lobe approximately ends at 0.25 T. Interestingly, it has been reported that the Josephson effect is observed with normal-metal electrodes in UBe_{13} point-contact. The origin is discussed as a proximitized normal layer or phase-slip [46, 47], and our observation may share the origin with that.
- [32] R. Kumar, G. Sheet, *Phys. Rev. B* **104**, 094525 (2021).
- [33] G. Sheet, S. Mukhopadhyay, P. Raychaudhuri, *Phys. Rev. B* **69**, 134507 (2004).
- [34] L. Aggarwal, *et al.*, *Nat. Mater.* **15**, 32 (2016).
- [35] L. Aggarwal, *et al.*, *Nat. Commun.* **8**, 13974 (2019).
- [36] F. Laube, G. Goll, H. v. Löhneysen, M. Fogelström, F. Lichtenberg, *Phys. Rev. Lett.* **84**, 1595 (2000).
- [37] C.-R. Hu, *Phys. Rev. Lett.* **72**, 1526 (1994).
- [38] Y. Tanaka, S. Kashiwaya, *Phys. Rev. Lett.* **74**, 3451 (1995).
- [39] D. Daghero, *et al.*, *Nat. Commun.* **786**, 786 (2012).
- [40] S. Sasaki, *et al.*, *Phys. Rev. Lett.* **107**, 217001 (2011).
- [41] W. Zhu, *et al.*, *Nat. Commun.* **14**, 7012 (2023).
- [42] G. E. Blonder, M. Tinkham, T. M. Klapwijk, *Phys. Rev. B* **25**, 4515 (1982).
- [43] M. Yamashiro, Y. Tanaka, S. Kashiwaya, *Phys. Rev. B* **56**, 7847 (1997).
- [44] D. Daghero, R. S. Gonnelli, *Supercond. Sci. Technol.* **23**, 043001 (2010).
- [45] A. P. Schnyder, P. M. R. Brydon, *J. Phys.: Condens. Matter* **27**, 243201 (2015).
- [46] E. L. Wolf, *et al.*, *J. Appl. Phys.* **61**, 3899 (1987).
- [47] A. M. Kadin, *Phys. Rev. B* **41**, 4072 (1990).

Supplementary Materials for

Probing p -wave superconductivity in UTe_2 via point-contact junctions

Hyeok Yoon, Yun Suk Eo, Jihun Park, Jarryd A. Horn, Ryan G. Dorman, Shanta R. Saha, Ian M. Hayes, Ichiro Takeuchi, Philip M. R. Brydon, Johnpierre Paglione

Correspondence to: paglione@umd.edu

This PDF file includes:

Figs. S1, S2 and S3

Captions for Figs. S1, S2, and S3

Table 1.

IV. THE FACETS OF SAMPLES

We use the anisotropy in the magnetic susceptibility χ to characterize the orientations of the UTe_2 crystals. For S1, the facets include the high-symmetry axis, as shown in Fig. S1. The facet of the junctions in S1 is parallel to a and b -axis and perpendicular to c -axis. On the other hand, for S2, the facet is not parallel to any of the high-symmetry axes. Therefore, we develop the way to find the facet as described below.

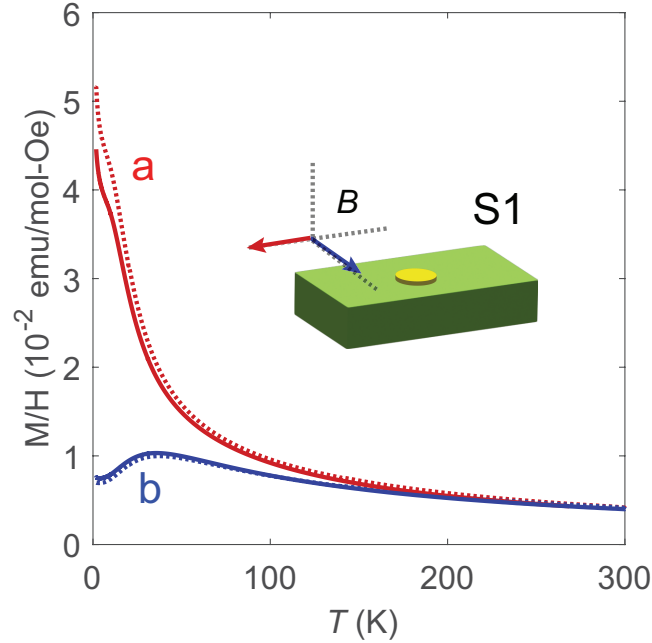


Fig. S1. The determination of the crystal orientation for S1. Two in-plane magnetic susceptibilities measured in S1 matched with χ_{aa} and χ_{bb} . Each B field direction is represented in the inset. Solid lines are our data in S1, and dotted lines are χ_{aa} , χ_{bb} , and χ_{cc} adopted from S. Ran, et al. [1].

Consider the initial principal axes of coordinates x, y, z corresponds to the a, b, c axis of UTe_2 crystal structure. Then, the magnetic susceptibility tensor can be represented as the following.

$$\chi = \begin{pmatrix} \chi_{aa} & 0 & 0 \\ 0 & \chi_{bb} & 0 \\ 0 & 0 & \chi_{cc} \end{pmatrix} \quad (2)$$

where χ_{aa} , χ_{bb} , χ_{cc} are the magnetic susceptibilities in a , b , c directions when the magnetic field B is applied in a , b , c directions, respectively. Their temperature dependence is reported in S. Ran et al. [1]. When the axes are rotated around z -axis by θ , the magnetic susceptibility in the new axes χ' can be represented as the following change of basis.

$$\chi' = \mathbf{R}_{z,\theta} \chi \mathbf{R}_{z,\theta}^T \quad (3)$$

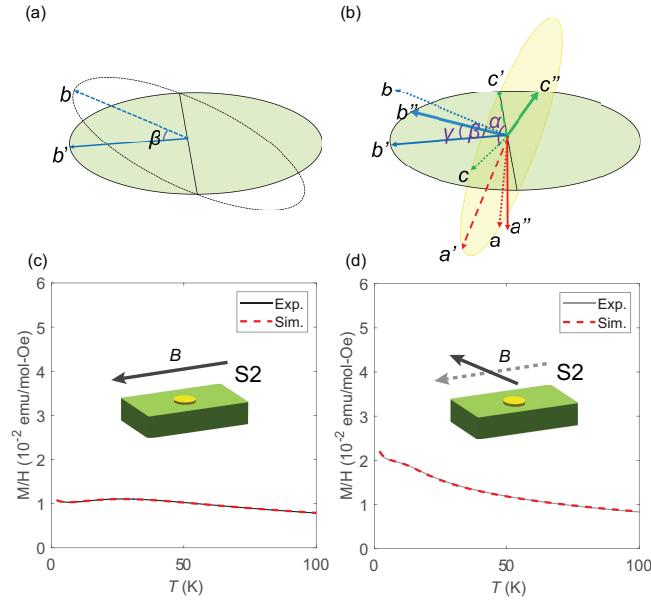


Fig. S2. The determination of the crystal orientation for S2. The schematic in Fig. S2(b) shows the step-by-step approach for this using YZX Euler's angles.

where the rotation matrix $\mathbf{R}_{z,\theta}$

$$\mathbf{R}_{z,\theta} = \begin{pmatrix} \cos \theta & -\sin \theta & 0 \\ \sin \theta & \cos \theta & 0 \\ 0 & 0 & 1 \end{pmatrix}$$

This representation in the new coordinate can be generalized to three rotations around y , z , and x axes with the Euler's angles α , β , and γ .

$$\chi' = \mathbf{R}_{x,\gamma} \mathbf{R}_{z,\beta} \mathbf{R}_{y,\alpha} \chi \mathbf{R}_{y,\alpha}^T \mathbf{R}_{z,\beta}^T \mathbf{R}_{x,\gamma}^T \quad (4)$$

In UTe_2 , the magnetic susceptibility along b -axis, χ_{bb} has a distinctive downturn below ~ 20 K whereas χ_{aa} and χ_{cc} -axis increase monotonically with decreasing temperature. Based on this fact, we first find the most b axis-like curve when B -field is applied in-plane, as shown in Fig. S2(c). Then, the real b -axis (b in Fig. S2(a)) lies just above the most b axis-like direction (b' in Fig. S1(a)) so that the plane including b and b' is perpendicular to the facet. By fitting the magnetic susceptibility in b' direction using eq. (3), we can find the angle $\beta = 17^\circ$ (Fig. S2(c)).

Next, in order to find a and c axis, we fit another curve measured with in-plane B field shown in Fig. S2(d). This is 41° degree off from the most b -like axis, and this is expected γ . Fitting the corresponding curve using eq. 4, results in $(\alpha, \beta, \gamma) = (67^\circ, 16^\circ, 33^\circ)$. β is nicely similar to the one obtained from Fig. S2, and γ is off by 8° from expectation. This can be converted to the normal vector of the facet $\hat{n} = [0.4, 0.6, 0.7]$. Considering the possible small misalignment in sample mounting, the results of the two fittings are quite consistent, indicating that this method of finding randomly oriented facets is reliable.

V. SAMPLE INFORMATION

Sample	Facet	Junction	Metal	Diameter	Wiring
S1	(001)	A	Ti(3 nm)/Au(150 nm)	340 μm	silver paste
		B	Ti(5 nm)/Au(150 nm)	340 μm	silver paste
S2	$\hat{n} = [0.4, 0.6, 0.7]$	A	Ti(3 nm)/Au(150 nm)	340 μm	Au wire bonding
		B	Ti(3 nm)/Au(150 nm)	340 μm	silver paste

TABLE I: Facets, counterelectrodes, diameters, and wiring methods for the junctions in S1 and S2.

VI. MAGNETIC FIELD DEPENDENCE IN S1-A.

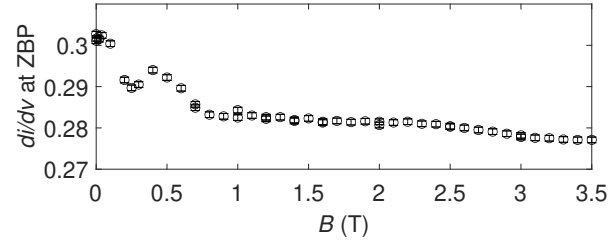


Fig. S3. Magnetic field dependence of the peak value of the zero-bias-peak (di/dv at ZBP) in S1-A.

VII. THEORY

We have utilized the generalized Blonder-Tinkham-Klapwijk (BTK) theory[38, 42] to model the conductance [44]. Specifically, the conductance is given by

$$\sigma(E) = \sigma_N \int \sigma_{\text{BTK}}(E' - i\Gamma) \left(-\frac{\partial f(E + E')}{\partial E'} \right) dE' \quad (5)$$

where σ_N is the normal-state conductance, $f(E)$ is the Fermi function, Γ is a phenomenological broadening parameter, and the normalized BTK conductance is given by

$$\sigma_{\text{BTK}}(E) = \int \left(1 - \frac{1}{2} \sum_{s,s'} (|b_{s,s'}(E, \Omega)|^2 - |a_{s,s'}(E, \Omega)|^2) \right) d\Omega. \quad (6)$$

Here $a_{s,s'}(E, \Omega)$ ($b_{s,s'}(E, \Omega)$) is the probability amplitude that a spin- s electron injected at angle Ω with energy E is Andreev (normal) reflected as a spin- s' hole (electron). In calculating these probability amplitudes we make a number of standard simplifying assumptions [44]: the Fermi surfaces in both materials are assumed to be spherical with the same radius k_F and isotropic effective mass m^* ; we model the interface by a δ -function potential of strength $\hbar^2 k_F Z / m^*$; and we neglect the variation of the gap near the surface. Relaxing these assumptions may alter the quantitative values of our fit parameters but is not expected to qualitatively alter our conclusions; in particular, the topological origin of the ZBP makes this feature immune to details of the system. The low crystal symmetry of UTe_2 places few restrictions on the structure of the pairing states in each irrep; to keep our task manageable we assume that the pairing state preserves time-reversal symmetry and we keep only the p -wave gap components in the most general pairing state for each irrep. Our fitting parameters hence consist of the relative strength of the different components, the overall gap amplitude Δ , the interface barrier strength Z , and the broadening parameter Γ .